

Stochastic Tomography and its Applications in 3D Imaging of Mixing Fluids

James Gregson*

Michael Krimerman

Matthias B. Hullin

Wolfgang Heidrich

University of British Columbia

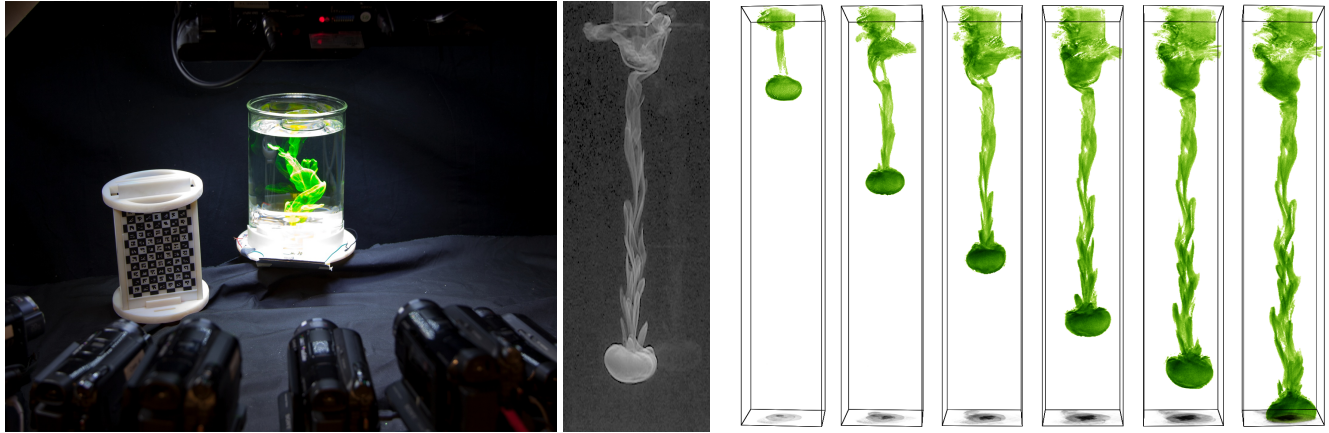


Figure 1: Left: Photo of an acquisition rig for fluid phenomena, consisting of 5–16 strobe-synchronized consumer cameras. Middle: Example capture of one of the cameras. Right: Reconstruction of an unsteady two-phase flow at different points in time. Note how the novel tomographic technique introduced in this paper manages to capture the fine-scale features in this challenging dataset. SAD regularizer, 100M sample mutations/frame, 6 min/frame.

Abstract

We present a novel approach for highly detailed 3D imaging of turbulent fluid mixing behaviors. The method is based on visible light computed tomography, and is made possible by a new stochastic tomographic reconstruction algorithm based on random walks. We show that this new stochastic algorithm is competitive with specialized tomography solvers such as SART, but can also easily include arbitrary convex regularizers that make it possible to obtain high-quality reconstructions with a very small number of views. Finally, we demonstrate that the same stochastic tomography approach can also be used to directly re-render arbitrary 2D projections without the need to ever store a 3D volume grid.

CR Categories: I.3.3 [COMPUTER GRAPHICS]: Picture/Image Generation—Digitizing and scanning;

Keywords: Stochastic sampling, Tomography, Fluid Imaging

Links: [DL](#) [PDF](#) [WEB](#) [VIDEO](#) [DATA](#)

* {jgregson|krim|hullin|heidrich}@cs.ubc.ca

1 Introduction

The capture of dynamic 3D phenomena has been the subject of considerable research in computer graphics, extending to both the scanning of deformable shapes, such as human bodies (e.g. [de Aguiar et al. 2007; de Aguiar et al. 2008]), faces (e.g. [Bickel et al. 2007; Alexander et al. 2009]), and garments (e.g. [White et al. 2007; Bradley et al. 2008]), as well as natural phenomena including liquid surfaces [Ihrke and Magnor 2004; Wang et al. 2009], gases [Atcheson et al. 2008], and flames [Ihrke and Magnor 2004]. Access to this kind of data is not only useful for direct re-rendering, but also for deepening our understanding of a specific phenomenon. The data can be used to derive heuristic or data-driven models, or simply to gain a qualitative understanding of what a phenomenon should look like before simulating it.

In this paper we focus on the capture of mixing processes between two liquids, as well as the dissolving of powdered dye into liquid. Like several other recent works [Ihrke and Magnor 2004; Ihrke et al. 2005; Atcheson et al. 2008], our capture process is based on visible light computed tomography (CT), which allows us to use inexpensive, off-the-shelf camera arrays. However, in addition to devising an effective capture setup for this specific problem, we also make significant algorithmic improvements to tomographic reconstruction techniques in general. In particular, we develop a new *stochastic* tomography algorithm that is especially well suited for the types of application scenarios encountered in graphics. Such applications typically have a relatively sparse set of views compared to more traditional settings for CT, such as medical imaging.

To our knowledge, Stochastic Tomography is the first CT algorithm that is both *matrix-free* and, by default, also *gridless*. Neither the tomography matrix nor the final volume grid need to be stored, which enables the reconstruction of larger, more detailed volumes than would be feasible with traditional methods. Moreover, we show

that our approach is straightforward to implement and can easily and seamlessly integrate additional convex regularization terms on an auxiliary grid. This also includes non-linear and non-smooth terms such as total variation (TV) or sum-of-absolute-differences (SAD). Our particular contributions are therefore as follows:

- We devise an inexpensive, practical setup for time-varying optical tomography of liquid mixing and dye immersion.
- We develop a novel *stochastic* tomographic reconstruction algorithm based on random walks inspired by Metropolis-Hastings sampling. This avoids spatial discretization of the reconstruction volume by representing the volume as a set of samples rather than a grid.
- We show how to incorporate arbitrary convex regularizers into the Stochastic Tomography framework using an auxiliary grid, and demonstrate the approach with both 3D and 2D sum-of-absolute-differences (SAD) regularizers. We show that these regularizers drastically improve the reconstruction quality compared to both unregularized Stochastic Tomography and standard methods such as SART [Andersen and Kak 1984], especially when considering setups with small numbers of cameras.
- We show that our Stochastic Tomography framework can also be used for re-rendering, i.e. the direct generation of novel projections without explicitly generating a 3D volume. We further demonstrate an image-space prior that improves the visual quality of renderings without requiring an auxiliary grid.

The remainder of this paper is structured as follows: in Section 2 we review the general computed tomography problem, as well as the specific image formation model for our liquid capture setup. We then discuss related work (Section 3) before describing the details of Stochastic Tomography (Section 4), including both 3D reconstruction and re-rendering. Section 5 details the experimental capture setup, with results being discussed in Section 6. We conclude with a discussion of other potential applications and future research directions (Section 7).

2 Computed Tomography

In this section we provide a concise introduction to traditional computed tomography, the specific image formation model relevant to our system, and the challenges associated with computed tomography based on visible light imaging.

2.1 The Tomographic Reconstruction Problem

Computed tomography is the process of reconstructing an unknown, volumetric, scalar signal from a collection of *line integrals* or *projections* taken through the signal using an *image-formation model* that describes the physics of the measurement process.

For our application, the image formation process can be modeled by an emissive volume, in which the light emitted by each point in a glowing or, in our case, fluorescing volume integrates along each line of sight (see Section 5 for details). More precisely, the (unknown) 3D volume is described by a continuous field $v(\mathbf{x})$ of light emissions. The volume is observed by a number of detectors i measuring the integral of the emissions along a ray Ω_i , (see Figure 2):

$$o_i = \int_{\Omega_i} v(\mathbf{x}) d\mathbf{x}. \quad (1)$$

In other settings, one may encounter light absorption (e.g. [Trifonov et al. 2006; Wetzstein et al. 2011b]) or more exotic image formation processes (e.g. [Atcheson et al. 2008; Lanman et al. 2011]), but even these models can usually be transformed into the form of Equation 1.

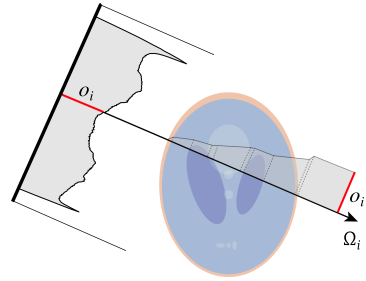


Figure 2: Measurement o_i is formed by the integral of the observed scene along the ray path Ω_i . The collection of measurements for each camera forms a projection image, the set of which from all cameras forms the input to our method.

Standard tomographic reconstruction techniques proceed by discretizing the unknown scalar field as $v(\mathbf{x}) \approx \sum_j v_j B_j(\mathbf{x})$ into basis functions $B_j(\mathbf{x})$ with a compact spatial support, typically arranged on a uniform grid of voxels. In this discrete setting, Equation 1 becomes

$$o_i = \mathbf{b}_i \cdot \mathbf{v}, \quad (2)$$

where the row vector \mathbf{b}_i consists of the coefficients of the linear equation describing the contribution of each voxel to the i^{th} ray according to the basis functions B_j , and \mathbf{v} is the vector of unknown emissivities for each voxel. Combining many such measurements yields a linear system, although the number of sensors does not typically exactly match the number of voxels. Consequently \mathbf{v} is estimated as the solution of the corresponding linear least-squares problem, which can be computed by a variety of methods [Kak and Slaney 2001]:

$$\mathbf{B}^T \mathbf{o} = \mathbf{B}^T \mathbf{B} \mathbf{v}. \quad (3)$$

2.2 Visible Light Tomography

The image formation model described above applies to both traditional CT problems, and the more recent applications in computer graphics. As an example, consider an array of calibrated cameras observing an emissive volume. Each pixel in each image corresponds to a known ray through the volume, and thus obtains a measurement modeled by Equation 1. After discretizing Equation 1 to obtain Equation 2, the coefficients of the row-vector \mathbf{b}_i model the integral of the projection of each basis function onto the ray Ω_i .

However, most computer graphics applications share several characteristics that distinguish them from traditional CT settings such as medical imaging. First, the number of cameras that can be used is typically about 8–16, far below the number of views used in medical CT. Although each individual camera may have high resolution, the sparse set of viewpoints means that the measurements are very unevenly spaced over the directional domain. As a direct consequence, additional priors and regularizers are usually required in order to obtain high resolution reconstructions from such data, leading, for example, to the development of visual hull constrained tomography in graphics [Ihrke et al. 2005].

Second, medical imaging often uses specific imaging geometries that allow slice-by-slice reconstruction of the volume, thus breaking the 3D reconstruction problem down into many 2D problems. This is typically not possible in visible light tomography settings, since camera ray geometries do not line up exactly in volume slices. Instead, the full 3D system needs to be solved at once, despite the 3D system typically being too big to store even as a sparse matrix. This rules out many standard linear solvers. Instead, CT often relies on *matrix-free* solvers such as simultaneous algebraic reconstruction tomography (SART, [Andersen and Kak 1984; Kak and Slaney

2001]), which represent the matrix procedurally in terms of volume rendering and backprojection operators. This approach solves the memory problem but makes it hard to incorporate the priors and regularizers required for reconstruction from sparse data, especially more powerful non-linear regularizers such as TV and SAD.

On a more fundamental level, imposing a discretization early on immediately imposes a fixed tradeoff between system size and reconstruction fidelity. In this paper we present a method for tomographic reconstruction employing stochastic random walks, which is straightforward to implement and is *gridless*. This allows the method to adaptively sample small features automatically. In addition, the design of our method makes it possible for tomographic reconstructions to be simultaneously computed and rendered *without storing volume data*.

In the event that gridded data is acceptable or desired, our method trivially incorporates state-of-the-art priors evaluated on an auxiliary grid. The ability to easily experiment with different regularization terms without a large development burden is a key advantage of our method. We believe that this will be particularly advantageous in graphics, where tomography has been used in a wide variety of applications, each of which may benefit from customized priors.

3 Related Work

The capture of dynamic phenomena has been an extremely prolific area of research in recent years. In this section we focus on work most directly related to ours: work in fluid capture, computed tomography, and Metropolis sampling.

Fluid Imaging is a very active research area in mechanical engineering. Most optical measurements in this community are performed with Particle Imaging Velocimetry [Grant 1997], which produces images of a single slice through the volume but has several shortcomings, such as the difficulty of injecting particles uniformly, and measuring out-of-plane flows. In computer graphics and machine vision, researchers have worked on imaging the surfaces of liquids [Morris and Kutulakos 2005; Ihrke et al. 2005; Wetzstein et al. 2011a], as well as volumetric smoke [Hawkins et al. 2005], flames [Hasinoff and Kutulakos 2007; Ihrke and Magnor 2004], and refracting gases [Atcheson et al. 2008]. In our work, we focus on imaging the mixing process of liquids, which is particularly interesting due to the fine-scale, turbulent structures that are formed. We note, however, that our stochastic tomography algorithm is general, and could be applied to other tomographic settings, such as the work by Atcheson et al. [2008].

Computed Tomography is another vast research area that we can only summarize briefly. For reasons outlined in Section 2, the state of the art in CT for general camera geometries are matrix-free iterative solvers such as SART [Andersen and Kak 1984], as well as regularized versions of these algorithms. Unfortunately, the specific structure of SART makes it difficult to implement sophisticated non-linear regularizers so regularized implementations of SART are often highly specialized to the regularization strategy, as in [Yu and Wang 2009].

One of the first links between tomography and probabilistic methods was due to Shepp and Vardi [1982], who discretized the domain into voxels and formulated the detection of photons in emission tomography as a maximum likelihood problem solved by an iterative method. Many have since extended this approach, particularly as the field seeks to limit the radiation doses received by patients, e.g. using new results from compressed sensing [Xu et al. 2011].

A work closely related to ours is that of Barbuza and Clausse [2011], where a voxelized reconstruction was generated

using a Metropolis-Hastings optimization for each voxel to minimize an energy function incorporating weighted L_2 smoothness constraints intended to promote sparsity. Our work extends this idea by allowing the random walk to choose the sample locations continuously in space, as well as their contribution to the image. This allows our method to concentrate effort on regions of the reconstruction which contribute most. In addition, we introduce true L_1 regularizers into the reconstruction, removing their need for thresholding of the smoothness energy.

Our method is also related to recent work on stochastic linear solvers (e.g. [Srinivasan and Aggarwal 2003; Srinivasan 2010]). However, unlike these general methods, we exploit the special geometric structure of tomography problems to derive a matrix-free stochastic solver. Since general tomography matrices tend to become very large—in the order of gigabytes—a matrix-free algorithm is of central importance for arriving at a practical method. Our matrix-free representation also allow us to easily incorporate general convex regularizers that make the overall system non-linear.

Finally, we note that computed tomography is emerging as a standard tool in graphics and vision. Besides 3D reconstruction [Hasinoff and Kutulakos 2007; Ihrke and Magnor 2004; Ihrke et al. 2005; Atcheson et al. 2008], tomography has recently been used for image generation on 3D displays [Wetzstein et al. 2011b; Lanman et al. 2011] and high dynamic range imaging [Rouf et al. 2011]. We believe that Stochastic Tomography could be of use for many of these applications.

Metropolis-Hastings Sampling [Metropolis et al. 1953; Hastings 1970] is a random walk algorithm that generates samples proportional to a probability distribution that only needs to support local evaluation. It is commonly used to perform difficult integrations stochastically (e.g. [Veach and Guibas 1997; Cline et al. 2005]), or as an efficient method to probe a parameter space in optimization (e.g. [Talton et al. 2011]). The advantage of the Metropolis-Hastings algorithm is that it generates efficient sampling patterns in scenarios where the underlying target probability distribution (PDF) for the samples can be evaluated, but it is not easily possible to draw samples proportional to it. Inspired by Metropolis-Hastings, we also use a random walk scheme. However, it is designed to minimize an objective function in a situation where the target PDF for the samples is not even available for evaluation. Therefore, despite its similarity, Stochastic Tomography is not truly Metropolis-Hastings sampling or even a Markov-Chain Monte Carlo method.

4 Stochastic Tomography

Instead of immediately discretizing Equation 1 like existing CT methods, we first define residuals r_i on the observations based on a current volume estimate \tilde{v}

$$r_i = o_i - \int_{\Omega_i} \tilde{v}(\mathbf{x}) d\mathbf{x}. \quad (4)$$

These residuals are then squared and summed over all measurements, and an (as yet unspecified) convex regularization function $\Gamma(\tilde{v}(\mathbf{x}))$ is added to obtain a convex objective function $F(\tilde{v}(\mathbf{x}))$:

$$F(\tilde{v}(\mathbf{x})) = \sum_i \left(o_i - \int_{\Omega_i} \tilde{v}(\mathbf{x}) d\mathbf{x} \right)^2 + \beta \Gamma(\tilde{v}(\mathbf{x})). \quad (5)$$

At this point it is useful to note that no spatial discretization has occurred except in taking discrete measurements, that the function $F(\tilde{v}(\mathbf{x}))$ is convex, and that (as before) the integral over Ω_i simply projects the approximation of the arbitrary field $\tilde{v}(\mathbf{x})$ onto the i^{th} measurement.

We would like to infer a volume estimate \tilde{v} that minimizes F . To do so, \tilde{v} is represented as a set of discrete samples $\{\mathbf{x}_k\} \propto \tilde{v}$, each of which deposits a certain amount of emissivity e_d . That is, \tilde{v} will be represented as the density of $\{\mathbf{x}_k\}$, and the task is to determine a sample set whose density estimate minimizes F .

To keep track of the improvement of the objective function during the sampling process, we define \tilde{v}_k to be the volume estimate after choosing the first k samples, and $\Delta F(\mathbf{x}_k) = F(\tilde{v}_{k-1}) - F(\tilde{v}_k)$ to be the change in the objective function due to a new sample \mathbf{x}_k . Note that $\Delta F(\mathbf{x}_k) > 0$ indicates that a sample \mathbf{x}_k improves on F .

4.1 Random Walk

A brute-force stochastic approach for minimizing Equation 5 would be rejection sampling: simply draw uniformly distributed random samples within the volume, and accept the sample if $\Delta F(\mathbf{x}_k) > 0$; discard it if not. Since our objective function is convex, and each accepted sample reduces the objective, clearly this simple strategy will converge eventually, albeit very slowly.

For a more practical approach, we turn to the Metropolis-Hastings algorithm [Metropolis et al. 1953; Hastings 1970] for inspiration to derive a new sampling strategy that explores areas with high payoff. In a similar fashion to Metropolis-Hastings, we perform a random walk that is based on mutating a current sample \mathbf{x}_{k-1} in order to propose a new sample \mathbf{x}_k . The proposed sample is accepted with some probability that depends on the improvement $\Delta F(\mathbf{x}_k)$ that it provides on the objective function. Pseudo-code for our Stochastic Tomography algorithm is provided in Algorithm 1.

Algorithm 1 Stochastic Tomography Random Walk

```

// Start the walk from a random point
 $\mathbf{x}_0 \leftarrow (\text{random}(), \text{random}(), \text{random}())^T$ 
for  $k \leftarrow 1$  to  $N$  do
    // New sample from  $\mathbf{x}_{k-1}$  and transition PDF  $t(\mathbf{x}_k | \mathbf{x}_{k-1})$ 
     $\mathbf{x}_k \leftarrow \text{sample}(\mathbf{x}_{k-1}, t(\mathbf{x}_k | \mathbf{x}_{k-1}))$ 
     $a \leftarrow \Delta F(\mathbf{x}_k) / \Delta F(\mathbf{x}_{k-1})$ 
    if  $\Delta F(\mathbf{x}_{k-1}) < 0$  or  $\text{random}() \leq a$  then
        // Record only samples that reduce the objective fn.
        if  $\Delta F(\mathbf{x}_k) > 0$  then
            // Incorporate the sample into the output
             $\text{record}(\mathbf{x}_k)$ 
        end if
    else
        // Keep exploring space from previous sample
         $\mathbf{x}_k \leftarrow \mathbf{x}_{k-1}$ 
    end if
end for

```

Instead of generating just a single random walk, we start multiple walks of length N from uniformly distributed random samples with the volume until a user-specified sample budget is exhausted. This process ensures *ergodicity*, i.e. that all points in the volume can be reached by the sampling process.

Convergence and Relationship to Metropolis-Hastings Despite the similarities of this process to Metropolis-Hastings, it is important to point out that the method does not produce a Markov Chain and consequently differs from Metropolis-Hastings sampling. Our sampling strategy explores local neighborhoods of samples that were previously successful in reducing the objective function, i.e. samples with $\Delta F > 0$. However, $\Delta F(\mathbf{x}_k)$ depends on the full sampling history, not just the previous sample \mathbf{x}_{k-1} . Second, we do not have a closed-form analytical representation of the target

PDF for the samples since our target PDF is the unknown volume estimate \tilde{v} that we seek to infer.

The convergence arguments outlined above for the brute-force rejection sampling approach still hold for the Stochastic Tomography algorithm since the objective function is convex and Stochastic Tomography i) fully explores the solution space (i.e. is ergodic) and ii) only accepts samples that reduce the objective function. Note that, unlike the original Metropolis-Hastings algorithm we do not require detailed balance to ensure convergence to the target solution.

Applying our random walk optimization strategy requires defining and implementing three problem-specific functions. First, we require the mutation strategy for generating a new sample from the previous one using a PDF $t(\mathbf{x}_k | \mathbf{x}_{k-1})$ for transitioning from one sample location to the next. Second, it is necessary to define an efficient way of estimating and updating $\Delta F(\mathbf{x}_k)$ of the objective function due to a new sample \mathbf{x}_k . Finally, we require a way to record accepted samples. We now discuss each aspect in turn.

Sample Mutation. The purpose of the mutation strategy is to choose a new sample location \mathbf{x}_k based on a current sample \mathbf{x}_{k-1} , and a transition probability $t(\mathbf{x}_k | \mathbf{x}_{k-1})$. The mutation strategy should favor samples that are most likely to improve the residual. In our case, this means exploring the neighborhood of the last successful sample (i.e. \mathbf{x}_{k-1}), which yields itself to a very simple mutation strategy that is highly effective: mutated samples are produced by simply adding a Gauss-distributed offset to each of the three coordinate directions. The width of the Gaussian is a user-specified parameter that affects the convergence rate but not the final solution, and we have found empirically that 5 – 10% of the diagonal of the reconstruction volume bounding box generally works well. Note that a Gaussian mutation strategy is symmetric (i.e. $t(\mathbf{x}_{k-1} | \mathbf{x}_k) = t(\mathbf{x}_k | \mathbf{x}_{k-1})$) and selects every point in the volume with a non-zero probability. The latter point means that even individual random walks are ergodic under this strategy. The new sample \mathbf{x}_k is then accepted with probability

$$a = \min(1, \frac{\Delta F(\mathbf{x}_k) t(\mathbf{x}_{k-1} | \mathbf{x}_k)}{\Delta F(\mathbf{x}_{k-1}) t(\mathbf{x}_k | \mathbf{x}_{k-1})}) = \min(1, \frac{\Delta F(\mathbf{x}_k)}{\Delta F(\mathbf{x}_{k-1})}), \quad (6)$$

so long as it also improves on the objective, i.e. $\Delta F(\mathbf{x}_k) > 0$.

Evaluating the Objective Function A key component of making our algorithm feasible is to find an efficient way to keep track of and evaluate $\Delta F(\mathbf{x}_k)$ for each newly proposed sample, which is illustrated in Figure 3. Ignoring regularizers (which are discussed in Section 4.3), this task can be reduced to keeping track of residual images \mathbf{r}_j for each of the M cameras, where the union of the M residuals represents Equation 4. This is essentially a density estimation problem in 2D, where new samples need to be added on the fly. A suitable algorithm is *kernel density estimation* [Parzen 1962], also known as *splatting*: if $\text{proj}_j(\mathbf{x}_k)$ projects sample point \mathbf{x}_k into the j^{th} residual image \mathbf{r}_j , while $\text{splat}_j(\mathbf{r}_j, \text{proj}_j(\mathbf{x}_k), e_d)$ splats e_d emissivity into \mathbf{r}_j and returns the resulting image, the change in Equation 5 due to the new sample is given as

$$\begin{aligned} \tilde{\mathbf{r}}_j^\pm &= \text{splat}(\mathbf{r}_j, \text{proj}_j(\mathbf{x}_k), \pm e_d) \\ \Delta_j^\pm F(\mathbf{x}_k) &= \mathbf{r}_j(\text{proj}_j(\mathbf{x}_k))^2 - \tilde{\mathbf{r}}_j^\pm(\text{proj}_j(\mathbf{x}_k))^2 \\ \Delta^\pm F(\mathbf{x}_k) &= \sum_j \Delta_j^\pm F(\mathbf{x}_k) \\ \Delta F(\mathbf{x}_k) &= \max(\Delta^+ F(\mathbf{x}_k), \Delta^- F(\mathbf{x}_k)). \end{aligned} \quad (7)$$

Note that we allow for samples of both positive and negative emissivity e_d . We check both signs of e_d when evaluating a sample's

contribution and take the sign which contributes the largest decrease in summed squared residuals over all images. This dramatically improves convergence by allowing the method to “rough-in” areas and refine them later (see Figure 6) and is also necessary for the regularizers (discussed in Section 4.3) to function properly.

We make one other minor optimization: if a sample \mathbf{x}_k falls outside the visual hull for any image (i.e. has a measured value of zero in at least one camera) it is automatically rejected. The rationale for this is that such samples cannot contribute to the final reconstruction and will require more work later on to undo, which can be avoided by simply not placing such samples in the first place.

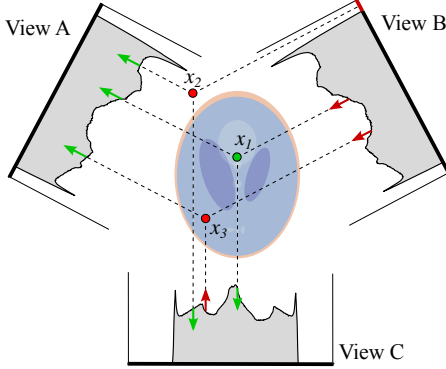


Figure 3: We evaluate how a given sample candidate affects the residual in the individual projections (views). Red arrows denote an increase of the residual, green arrows a decrease. Sample x_1 contributes a net decrease of the overall residual error, and is therefore accepted. Sample x_2 would also decrease the error function, but lies outside the visual hull of View B, hence, it is rejected. Sample x_3 delivers a net increase in error, therefore it is rejected as well.

Storing Samples in Residuals When a sample \mathbf{x}_k is accepted by the Stochastic Tomography sampler, it must somehow be incorporated into the reconstruction. Our method does this by splatting $\pm e_d$ of emissivity (with the sign chosen according to largest decrease of Equation 5) into the residual images \mathbf{r}_j at \mathbf{x}_k ’s projected points. We perform this splatting with bilinear weights due to the compact support.

$$\mathbf{r}_j = \text{splat}(\mathbf{r}_j, \text{proj}_j \mathbf{x}_k, \pm e_d) \quad (8)$$

In addition to storing the sample in the residual images, we also need to post-process them to derive the desired volume data. We can either process the samples on the fly, or save them to disk and process them at a later point in time.

Choosing e_d and Number of Samples Our algorithm has several inter-related parameters that must be specified prior to starting a reconstruction. The deposition emissivity e_d is the quantized emissivity per sample, N is the number of sample mutations per sampling chain, and Γ is the total number of sampling chains to start. We have found that the method is relatively insensitive to the sample chain length N , and have used values ranging from 1000 to 20000 with success. After choosing N the remaining parameters are related by the following expression

$$\Gamma = \alpha \frac{e_{tot}}{N e_d} \quad (9)$$

where e_{tot} is the total observed emissivity, obtained by averaging the sum of measurements o_i over all cameras and α is scale factor to account for the fact that not all samples are accepted. The choice

α is somewhat data-dependent, but values in the range of $10 - 40$ work well.

The user must then choose either the deposition emissivity e_d , or number of sampling chains Γ . The choice of one uniquely determines the other. If the range of emissivity field values are known approximately, choosing e_d directly controls the quantization level and is preferred for that reason. Otherwise, choosing Γ will directly bound computation time by only considering ΓN samples.

4.2 Sample Processing

The sample-based representation of the volume supports several ways of post-processing, detailed below.

Volume Reconstruction. The reconstruction of a 3D volume from samples is a density estimation problem. In our implementation, we again choose a simple kernel density estimation approach [Parzen 1962], in which the samples are splatted onto a regular volume grid using trilinear weights, again for compact support. However, we note that a sample-based representation also lends itself to adaptive reconstructions, for example using hierarchical data structures such as an octree to represent the final volume. Note that density estimation on an adaptive grid is potentially more efficient than performing standard matrix-free iterative solvers such as SART on adaptive grids. It is also possible to employ more sophisticated density estimation algorithms, although the advantage of kernel density estimation is that the samples can be splatted independently, and then discarded.

2D Re-rendering. If the ultimate goal is to simply render images of the volume from novel viewpoints that are known *a priori*, then the samples can be directly re-projected, and the density estimated in 2D only. If we once again use kernel density estimation, we can directly re-render any number of novel views without ever storing either the 3D volume or more than one sample at a time.

Per-slice Reconstructions. For sake of completeness, we mention that it is possible to use precomputed samples to reconstruct individual 2D slices through a volume on-the-fly in an interactive system. We believe this option may be of interest when applying Stochastic Tomography in a medical imaging setting.

4.3 Regularization

In the discussion so far, the objective function for the random walk algorithm was given directly by the linear system derived from the tomographic image formation model. This simple objective function may not be sufficient if the observed measurements are very sparse or noisy. In this case it is necessary to incorporate prior information about the data to be reconstructed, in the form of a regularization term $\Gamma(\tilde{v})$ (see Equation 5).

While the best choice of regularizer depends on the nature of the problem, Stochastic Tomography supports any convex regularizer with relatively compact support to be introduced simply and efficiently. The convexity restriction ensures that the method finds the true global minimum at the limit of number of samples and deposition emissivity e_d , while compact support is a more practical restriction needed since the change in regularization term will be evaluated once per sample. The regularization terms are simply added to Equation 5, and are evaluated by the sampling procedure in the same manner as the objective function: by computing the difference in energy caused by accepting the sample. This energy difference is simply added to the $\Delta F(\mathbf{x}_k)$ value returned by the objective function.

To illustrate the flexibility of our method, we have implemented several different regularizers, one based on a smoothness energy, two L_1 sparse-gradient priors and a third which operates only on output rendered projections, allowing our method to operate entirely without volume data.

Volume-based Regularization. If the goal is the reconstruction of a 3D volume, we can incorporate regularizers by performing density estimation on a 3D grid (Section 4.2) on the fly during the random walk. This grid-based volume representation can then be used to estimate how a new sample would affect the gradients in the volume. In our work we have implemented three grid-based priors, an L_2 smoothness energy, an L_1 Sum-of-Absolute-Differences (SAD) energy and an L_1 Total Variation (TV) energy.

If \tilde{v}_{k-1} is the volume estimate after placing $k-1$ samples, and \tilde{v}_k the estimate after splatting sample \mathbf{x}_k , then the regularization energy change $\Gamma(\mathbf{x}_k)$ due to a regularization function $\gamma(\cdot)$ is:

$$\Gamma(\mathbf{x}_k) = \gamma(\tilde{v}_k) - \gamma(\tilde{v}_{k-1}) \quad (10)$$

All regularizers are evaluated on stencils centered at the sample, with spacing equal to the grid spacing. The L_2 regularizer energy is evaluated with a standard 7-point (in 3D) Laplacian stencil, the result of which is squared, while the TV regularizer energy returns the gradient magnitude, computing each component with first-order finite-differences. The SAD regularizer sums the absolute difference between the center sample and each of the 26 neighboring samples in a $3 \times 3 \times 3$ window.

In our stochastic framework, it is straightforward to swap one type of regularizer for another, which makes it easy to experiment with different kinds of regularization (also see Section 6). This is in stark contrast to the use of non-linear regularizers in standard optimization techniques, where different solvers need to be developed for each type of regularization (e.g. [Yu and Wang 2009]).

Image-space Regularization. If the final goal is to render into novel viewpoints, the regularization can also be performed directly in 2D image space. This way, we can maintain the grid-free nature of the re-rendering algorithm (Section 4.2). We can use 2D variants of any of the 3D regularizers discussed for the volume case, and apply them directly on the generated output images. The total regularizer value is then the sum of all individual image regularizers.

As will be shown in Section 6, the image-space regularization succeeds in increasing the visual fidelity of images generated with the re-rendering approach. It may seem that, instead of this image-space regularization, similar results could be accomplished by filtering as a post-processing step. This is not the case: by adding output-quality terms to our reconstruction, we bias the method to produce solutions from the indefinite problem that satisfy the measurements while also producing a smooth output, while any smoothing as a post-process would yield results that are no longer consistent with the measurements.

We also experimented with using only image-space regularizers to improve the 3D grid reconstruction, but found that the 2D regularization even for a relatively large number of novel image views is not sufficiently strong to yield significant quality improvements for the 3D volume.

5 Experimental Setup

To apply our stochastic tomography algorithm to the problem of reconstructing 3D animated volumes of mixing fluids, we devised an experimental setup to capture such data (Figures 1 and 4). At the heart of the setup, we have a cylindrical glass beaker similar to

the one used by Trifonov et al. [2006], which is used to contain the liquids used in the experiments. Observing this setup are between 5 and 15 Sony consumer camcorders. The per-pixel ray geometries for each camera are calibrated with the two-plane approach proposed by Trifonov et al.



Figure 4: Photograph of the experimental setup. An array of 5–15 consumer camcorders arranged in a semicircle focuses on a water-filled glass beaker containing the reconstruction volume. A two-plane calibration procedure is used to obtain ray-pixel correspondences within the capture volume. Fluorescein-sodium fluorescent dye is then introduced, either as a powder or mixed with water or isopropyl alcohol, from the top of the beaker, or by injection through a tube into the bottom of the capture volume.

During the experiments, we mixed a clear liquid (typically water) with a second liquid to which fluorescein-sodium, a fluorescent dye, had been added. This second, dyed fluid was either water or isopropyl alcohol. In some experiments we also directly imaged the insertion of un-dissolved dye into water.

Illumination. We used white LED strobes, which provide us with the ability to optically synchronize the cameras for imaging fast-moving effects [Bradley et al. 2009]. For slow moving effects we were able to use constant illumination from ultra-violet LEDs, which provide better contrast at reduced stray light, but only frame-level camera synchronization. In both cases we assume an image formation model where light from the illuminant is absorbed and isotropically re-emitted by the fluorescent dye. By neglecting re-absorption of the visible light on the path to the camera, we arrive at the emission tomography image formation model from Equation 1. We note, however, that the intensity incident in each voxel varies based on the distance of the voxel from the illuminant, as well as any volumetric shadowing that may occur on the way from the illuminant to the voxel. Therefore, our capture setup allows for *qualitative* imaging of fluid mixing; a quantitative mapping from measured intensities to dye concentrations is not currently possible.

Radiometric calibration. In order to compare measurements between camera views, we perform a straightforward radiometric calibration process that starts by lighting the calibration target plane positions from [Trifonov et al. 2006] consistently using a calibration ‘headlight’. This is the only illumination used during calibration, ensuring that the target plane is lit consistently from all views. After applying an inverse gamma curve to the captured calibration images, we designate one camera the master and find an exposure scale factor for all other cameras that minimizes the luminance differences for a set of corresponding points on the calibration plane between each view and the master. These factors are then applied to all frames from a given camera. Finally, portions of the image falling outside the calibrated region are set to zero. The input projection data (i.e. the measurement vector \mathbf{o}) is then computed by subtracting a background image from each captured frame.

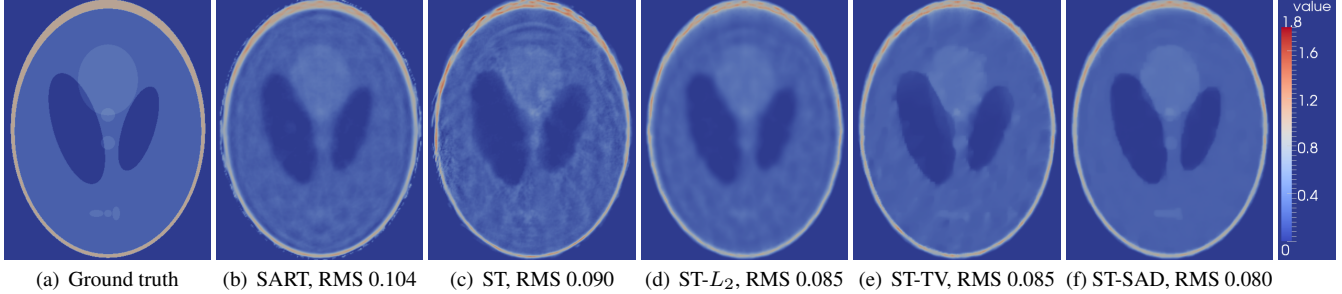


Figure 5: Reconstruction of the high-contrast Shepp-Logan phantom (a), a standard medical-imaging test-case, from 16 orthographic views using SART (b) and Stochastic Tomography (ST) (c)–(f) on an 256×256 output grid (stochastic tomography results accumulated as in Section 4.2). All results are shown in the same scale and have runtimes between 47 and 55 seconds. RMS errors with respect to ground truth are also provided.

6 Results

In the following we present results obtained using Stochastic Tomography, both for standard tomography test cases and for data captured using our optical tomography acquisition setup.

6.1 2D Synthetic Data

We start with a comparison of a reconstruction using the Simultaneous Algebraic Reconstruction Technique (SART) of Andersen and Kak [1984] to several generated by Stochastic Tomography. We chose to compare to SART because it produces reasonably high-quality reconstructions while still being applicable to arbitrary camera models. SART can also form the basis of several more sophisticated regularized methods, such as [Yu and Wang 2009].

Figure 5 shows the results for reconstructing the ubiquitous Shepp-Logan phantom from 16 orthographic cameras on a 256×256 output grid. This is a very challenging task for CT algorithms since the limited number of views causes the linear system to be drastically under-determined. In the interest of a fair comparison, we have adjusted the parameters of Stochastic Tomography to achieve a runtime smaller than the SART computation time. We also added the visual-hull constraint of Atcheson et al. [2008] to the SART implementation. The basic, unregularized Stochastic Tomography result (Figure 5(c)) shows artifacts that are structurally similar but more pronounced than the one produced by SART (b); SART selects a smoother solution from the null-space of the linear system.

This situation changes once we add regularizers to Stochastic Tomography. The L_2 regularizer removes the majority of artifacts but blurs hard edges (Figure 5(d)), producing reconstructions comparable to SART in quality. The L_1 TV regularizer (e) improves the sharpness of the result but still has prominent artifacts, while the SAD regularizer (f) preserves the sharp edges and details of the phantom best.

We have computed the RMS errors of our reconstructions with respect to the ground truth, and found that as expected, the SAD regularizer performs the best with an RMS error of 0.080 as compared to the unregularized RMS error of 0.090. Somewhat surprising is that the unregularized Stochastic Tomography results have a lower RMS error than the SART results, in spite of being visually less appealing. The very small number of cameras in this example cause the visual hull to have a polygonal shape, and SART ends up depositing energy in the gaps between this visual hull and the true elliptical shape. The Stochastic Tomography methods, for reasons that will require further investigation, appears to be less sensitive to this situation and do not produce the same artifacts.

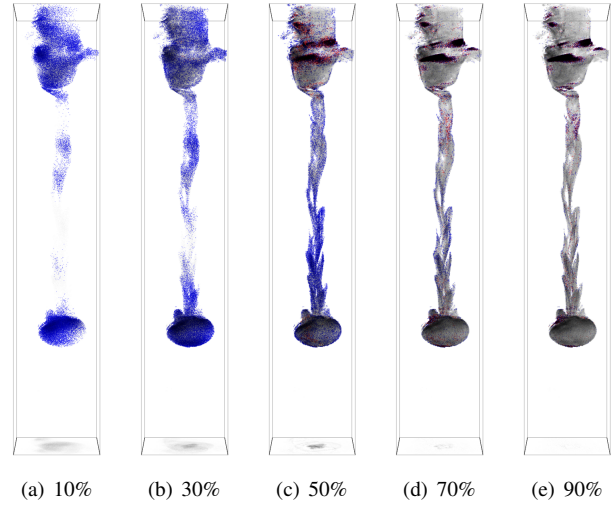


Figure 6: Illustration of the sampling process at work for varying levels of completion. Positive samples are drawn in blue, negative samples in red. The algorithm first roughs-in the reconstruction with positive samples, then refines it using negative samples.

Although it is possible to create regularized versions of SART (e.g as demonstrated by Yu and Wang [2009]), we note that changing regularizers for SART and other linear solvers requires a complete re-implementation of the solver, while it is straightforward to replace regularizers in Stochastic Tomography. This property allows us to quickly test different kinds of regularization for a specific problem and select the one that produces the best results for a given application domain.

6.2 3D Capture of Mixing Fluids

We now turn to the reconstruction of real datasets of mixing fluids obtained using the experimental setup of Section 5. To illustrate the potential of our approach, we cover a range of different types of fluid interactions, including thin, quasi-stable flows, as well as turbulent behavior arising from pouring and buoyancy. We strongly encourage the reader to refer to the supplemental video for the full animated sequences. All reconstructions were performed on a single core of an Intel i7 desktop. Sample budget and timings are listed in the figure captions. Figure 1 shows several timesteps from a capture of fluorescein-sodium dye in water being dropped approximately 1cm through a thin tube into still water. As the dyed fluid

enters the still water, a quasi-stable vortex is formed which propagates downwards, slowing and developing capillary waves which form a complex petal-like pattern on the vortex trail. Stochastic Tomography is able to capture fine-scale, transient features of this flow; please see the supplemental video for the corresponding animated sequence. This reconstruction used 100 million sample mutations with 65000 sampling chains from 16 cameras regularized with grid-based SAD. In Figure 6 we show the reconstruction of one frame from this sequence at varying levels of completion to illustrate the placement of positive (blue points) and negative samples (red points). The method starts by placing a large number of positive samples to quickly rough-in the scene. It then refines this coarse approximation by placing a mixture of positive and negative samples.

Figure 7 shows a comparison between one of the input images and a grid-free re-rendering from a similar viewpoint for an alcohol-and-fluorescein-sodium mixture being injected into the bottom of the reconstruction volume and rising under buoyancy. Stochastic Tomography captures much of the fine-scale detail of the transition from laminar to turbulent flow both spatially and over time. Such turbulent details and dynamics are challenging to simulate realistically, but can be captured easily with our setup and potentially used to develop data-driven models for future simulations. We show a series of renderings of this data from artificial views in Figure 9. This dataset also shows a shortcoming of our specific capture setup: reflections of the emissive volume can occur in the back wall of the glass beaker (Figure 7). If these reflections are consistent across cameras and cannot be properly separated from the actual volume data, they can introduce some artifacts in the final reconstruction, for example in Figure 9(d), where isolated patches are erroneously reconstructed.



Figure 7: 95% isopropyl alcohol and fluorescein-sodium rising under buoyancy after injection into standing tap-water. Camera view (left) and grid-free stochastic tomography reconstruction (right) from 15 views re-rendered from a similar viewpoint. Many fine scale features of the transition from laminar-flow to turbulent-mixing are captured by the rendering, however minor camera misalignment limits the reconstruction resolution. Please see the supplemental material for the corresponding animated sequence. This reconstruction used 200 million mutations and 10 thousand sample chains with no regularization. Computation time: 14 min/frame.

Figure 10 shows novel viewpoints of a diluted fluorescein-sodium solution being poured into still tap water. Small eddies form almost immediately, which then diffuse and grow over time. Each frame was reconstructed by our stochastic tomography method from 9 cameras using 400 million sample mutations and the grid-based SAD regularizer on a 200^3 grid.

An extreme example of a reconstruction from just 5 cameras is shown in Figure 8. In this capture, fluorescein-sodium dye powder was introduced to the water surface and allowed to mix and dissolve. On this dataset, we demonstrate the difference between regularized and unregularized Stochastic Tomography using a very coarse sampling to exaggerate the differences. The left image of Figure 8 shows the result using our image-based SAD regularizer. The right column shows the difference between the unregularized reconstruction (top inset), the grid-based SAD regularizer (center inset) and the image-based SAD regularizer (bottom inset). The regularized results show a clear improvement of output image-quality over the unregularized case, with the differences between the volume-based and image-based regularization being minimal. This allows high-quality, regularized renderings of volume data to be performed on the fly, without any volume data being stored.

7 Conclusions and Future Work

In this paper we have introduced Stochastic Tomography, a new random walk algorithm for tomographic reconstruction of 3D volumes. The key advantages of this approach are the avoidance of spatial discretization, which allows us to represent the reconstructed volume in a grid-free fashion without a fixed resolution tradeoff, and the ease with which arbitrary convex but potentially non-linear regularizers and priors can be incorporated into the reconstruction. As we have shown, together these properties of Stochastic Tomography allow us to push the state of the art in tomographic reconstruction of detailed volumes from a very small number of input views.

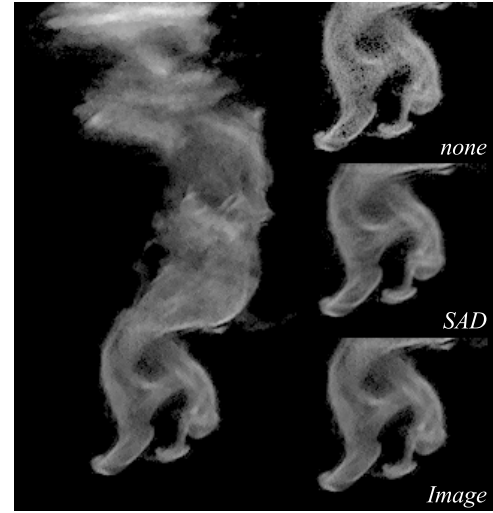


Figure 8: Deliberately undersampled reconstruction of dye-powder added to the surface of the capture volume from only 5-cameras using image-based regularization (left). The right column shows a comparison of regularization strategies. From top to bottom: Unregularized result, regularized with SAD, and with image-based SAD. The image-based regularization can produce results comparable to grid-based regularization for output-renderings, but does not require volume data.

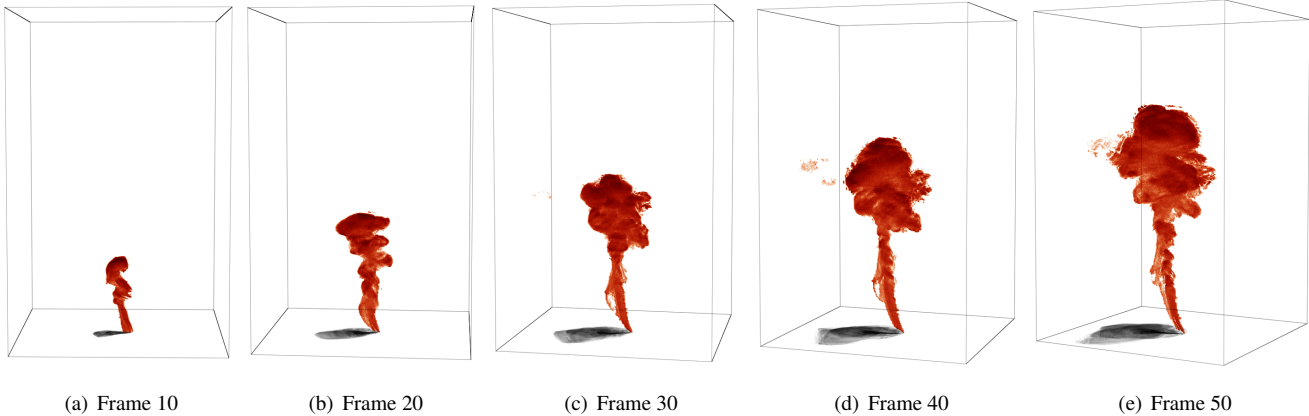


Figure 9: Buoyancy-driven flow of fluorescein-alcohol solution in water. 200M mutations/frame, 14 min/frame.

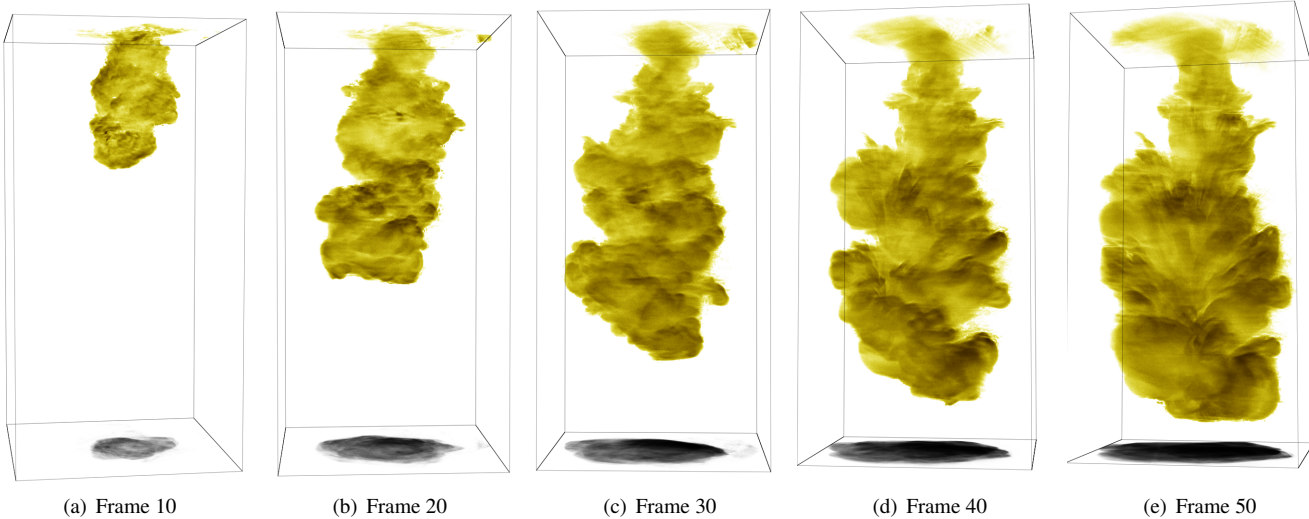


Figure 10: Time-resolved reconstruction of diluted fluorescein-sodium being poured into still tap water. Complex vortices and eddies develop as the fluid propagates. 400 million mutations and 10 thousand sampling chains were used with the SAD regularizer. Computation time: 31 min/frame.

We also have shown how this new reconstruction approach can be applied to the detailed imaging of complex fluid mixing behaviors. As mentioned in Section 5, currently our results are qualitative rather than quantitative, since we do not account for spatial variations of the incident illumination at each point in the volume. The setup itself also has several other shortcomings, such as the tendency to produce reflections that can pollute the measurements (Section 6). In the future we would like to explore variations of this setup, for example with anti-reflective coating, or out-of-plane cameras that eliminate the reflection problem. We want to expand on the number and type of mixing effects, and would like to be able to recover effects such as the transition from laminar to turbulent flows in tubes, for example.

On the algorithmic side, Stochastic Tomography can be thought of as a fixed step-length stochastic subgradient descent method. In future work, we would like to consider adapting the method to alternative, stochastic optimization methods, with the aim of improving the efficiency of reconstruction. Furthermore, Stochastic Tomogra-

phy currently uses non-linear regularizers, but the data term itself is linear, in accordance with the image formation model introduced in Section 2. In the future, we would like to explore the possibility to use convex, but possibly non-linear data terms. For example, both emission and absorption tomography can individually be formulated as linear problems, but the combined emission/absorption problem is non-linear, yet still convex. It would be interesting to solve these kinds of problems with Stochastic Tomography. This would also provide an avenue for recovering actual quantitative dye concentrations from our measurement setup.

Another promising avenue for future research is the expansion of the system to the temporal domain. By sampling particles in a 6D state space consisting of position and velocity, and computing residuals in successive time steps, one could attempt to generate tracked particles directly in the reconstruction, rather than a separate post-processing step. We believe that this can serve as a way to transition from measuring per-frame dye concentrations to measuring fluid motion.

Despite some shortcomings in the current capture setup, we believe our fluid mixing results show many interesting details and intricate behavior currently difficult to generate with fluid simulators used in computer graphics. In addition to providing specific datasets for a computer animation, we believe that capture techniques such as ours play an important role in understanding natural phenomena, and can provide data to further enhance simulation algorithms. All of our datasets will be made publicly available for this purpose.

References

- ALEXANDER, O., ROGERS, M., LAMBETH, W., CHIANG, M., AND DEBEVEC, P. 2009. The Digital Emily project: photoreal facial modeling and animation. In *SIGGRAPH Courses*, 1–15.
- ANDERSEN, A., AND KAK, A. 1984. Simultaneous algebraic reconstruction technique (SART): A superior implementation of the ART algorithm. *Ultrasonic Imaging* 6, 1, 81 – 94.
- ATCHESON, B., IHRKE, I., HEIDRICH, W., TEVS, A., BRADLEY, D., MAGNOR, M., AND SEIDEL, H.-P. 2008. Time-resolved 3D capture of non-stationary gas flows. *ACM Trans. Graph. (Proc. SIGGRAPH Asia)* 27, 5, 132.
- BARBUZZA, R., AND CLAUSS, A. 2011. Metropolis Monte Carlo for tomographic reconstruction with prior smoothness information. *Image Processing, IET* 5, 2 (Mar.), 198 –204.
- BICKEL, B., BOTSCHE, M., ANGST, R., AND MIGUEL OTADUY, W. M., PFISTER, H., AND GROSS, M. 2007. Multi-scale capture of facial geometry and motion. *ACM Trans. Graph. (Proc. SIGGRAPH)*, 33.
- BRADLEY, D., POPA, T., SHEFFER, A., HEIDRICH, W., AND BOUBEKEUR, T. 2008. Markerless garment capture. *ACM Trans. Graph. (Proc. SIGGRAPH)* 27, 3, 99.
- BRADLEY, D., ATCHESON, B., IHRKE, I., AND HEIDRICH, W. 2009. Synchronization and rolling shutter compensation for consumer video camera arrays. In *Proc. PROCMAS*.
- CLINE, D., TALBOT, J., AND EGBERT, P. 2005. Energy redistribution path tracing. *ACM Trans. Graph.* 24 (July), 1186–1195.
- DE AGUIAR, E., THEOBALT, C., STOLL, C., AND SEIDEL, H.-P. 2007. Marker-less deformable mesh tracking for human shape and motion capture. In *Proc. CVPR*.
- DE AGUIAR, E., STOLL, C., THEOBALT, C., AHMED, N., EIDEL, H.-P. S., AND THRUN, S. 2008. Performance capture from sparse multi-view video. *ACM Trans. Graph. (Proc. SIGGRAPH)*.
- GRANT, I. 1997. Particle image velocimetry: A review. *J. Mech. Eng. Science* 211, 1, 55–76.
- HASINOFF, S., AND KUTULAKOS, K. 2007. Photo-Consistent 3D Fire by Flame-Sheet Decomposition. *IEEE Trans. PAMI* 29, 5, 870–885.
- HASTINGS, W. K. 1970. Monte Carlo sampling methods using Markov chains and their applications. *Biometrika* 57, 1, 97–109.
- HAWKINS, T., EINARSSON, P., AND DEBEVEC, P. 2005. Acquisition of Time-Varying Participating Media. *ACM Trans. Graph. (Proc. SIGGRAPH)* 24, 3, 812–815.
- IHRKE, I., AND MAGNOR, M. 2004. Image-Based Tomographic Reconstruction of Flames. In *Proc. SCA*, 367–375.
- IHRKE, I., GOLDLUECKE, B., AND MAGNOR, M. 2005. Reconstructing the Geometry of Flowing Water. In *Proc. ICCV*, 1055–1060.
- KAK, A. C., AND SLANEY, M. 2001. *Principles of computerized tomographic imaging*. SIAM.
- LANMAN, D., WETZSTEIN, G., HIRSCH, M., HEIDRICH, W., AND RASKAR, R. 2011. Polarization fields: Dynamic light field display using multi-layer LCDs. *ACM Trans. Graph. (Proc. SIGGRAPH)* 30, 6.
- METROPOLIS, N., ROSENBLUTH, A. W., ROSENBLUTH, M. N., TELLER, A. H., AND TELLER, E. 1953. Equation of state calculations by fast computing machines. *J. Chem. Phys.* 21, 6, 1087–1092.
- MORRIS, N. J. W., AND KUTULAKOS, K. N. 2005. Dynamic refraction stereo. In *Proc. ICCV*, 1573–1580.
- PARZEN, E. 1962. On estimation of a probability density function and mode. *Ann. Math. Stat.* 33, 1065–1076.
- ROUF, M., MANTIUK, R., HEIDRICH, W., TRENTACOSTE, M., AND LAU, C. 2011. Glare encoding of high dynamic range images. In *Proc. CVPR*.
- SHEPP, L. A., AND VARDI, Y. 1982. Maximum likelihood reconstruction for emission tomography. *IEEE Trans. Med. Imag.* 1, 2 (Oct.), 113 –122.
- SRINIVASAN, A., AND AGGARWAL, V. 2003. Stochastic linear solvers. In *Proc. SIAM Conf. Applied Linear Algebra*.
- SRINIVASAN, A. 2010. Monte Carlo linear solvers with non-diagonal splitting. *Mathematics and Computers in Simulation* 80, 6, 1133–1143.
- TALTON, J., LOU, Y., LESSER, S., DUKE, J., MĚCH, R., AND KOLTUN, V. 2011. Metropolis procedural modeling. *ACM Trans. Graph.* 30, 2 (April).
- TRIFONOV, B., BRADLEY, D., AND HEIDRICH, W. 2006. Tomographic Reconstruction of Transparent Objects. In *Proc. EGSR*, 51–60.
- VEACH, E., AND GUIBAS, L. J. 1997. Metropolis light transport. In *Computer Graphics (Proc. SIGGRAPH '97)*, 65–76.
- WANG, H., LIAO, M., ZHANG, Q., YANG, R., AND TURK, G. 2009. Physically guided liquid surface modeling from videos. *ACM Trans. Graph.* 28 (July), 90:1–90:11.
- WETZSTEIN, G., HEIDRICH, W., AND RASKAR, R. 2011. Refractive shape from light field distortion. In *Proc. ICCV*.
- WETZSTEIN, G., LANMAN, D., HEIDRICH, W., AND RASKAR, R. 2011. Layered 3D: Tomographic image synthesis for attenuation-based light field and high dynamic range displays. *ACM Trans. Graph.* 30, 4.
- WHITE, R., CRANE, K., AND FORSYTH, D. 2007. Capturing and animating occluded cloth. *ACM Trans. Graph. (Proc. SIGGRAPH)*, 34.
- XU, Q., MOU, X., WANG, G., SIEREN, J., HOFFMAN, E., AND YU, H. 2011. Statistical interior tomography. *IEEE Trans. Med. Imag.* 30, 5 (May), 1116 –1128.
- YU, H., AND WANG, G. 2009. Compressed sensing based interior tomography. *Physics in medicine and biology* 54, 2791.